

Research Paper

Mechanically induced integrin ligation mediates intracellular calcium signaling with single pulsating cavitation bubbles

Fenfang Li^{1,3}, Tae Hyun Park¹, George Sankin¹, Christopher Gilchrist², Defei Liao¹, Chon U Chan⁴, Zheng Mao¹, Brenton D. Hoffman², Pei Zhong¹

1. Department of Mechanical Engineering and Materials Science, Duke University, Durham, NC 27708.
2. Department of Biomedical Engineering, Duke University, Durham, NC 27708.
3. Lee Kong Chian School of Medicine, Nanyang Technological University Singapore, Singapore, 308232.
4. Institute of Molecular and Cell Biology, Agency for Science, Technology and Research (A*STAR), Singapore, Singapore.

✉ Corresponding authors: fenfang.li@duke.edu (F.L.), brenton.hoffman@duke.edu (B.H.), pzhong@duke.edu (P.Z.).

© The author(s). This is an open access article distributed under the terms of the Creative Commons Attribution License (<https://creativecommons.org/licenses/by/4.0/>). See <http://ivyspring.com/terms> for full terms and conditions.

Received: 2020.12.05; Accepted: 2021.03.23; Published: 2021.04.07

Abstract

Therapeutic ultrasound or shockwave has shown its great potential to stimulate neural and muscle tissue, where cavitation microbubble induced Ca^{2+} signaling is believed to play an important role. However, the pertinent mechanisms are unknown, especially at the single-cell level. Particularly, it is still a major challenge to get a comprehensive understanding of the effect of potential mechanosensitive molecular players on the cellular responses, including mechanosensitive ion channels, purinergic signaling and integrin ligation by extracellular matrix.

Methods: Here, laser-induced cavitation microbubble was used to stimulate individual HEK293T cells either genetically knocked out or expressing Piezo1 ion channels with different normalized bubble-cell distance. Ca^{2+} signaling and potential membrane poration were evaluated with a real-time fluorescence imaging system. Integrin-binding microbeads were attached to the apical surface of the cells at mild cavitation conditions, where the effect of Piezo1, P2X receptors and integrin ligation on single cell intracellular Ca^{2+} signaling was assessed.

Results: Ca^{2+} responses were rare at normalized cell-bubble distances that avoided membrane poration, even with overexpression of Piezo1, but could be increased in frequency to 42% of cells by attaching integrin-binding beads. We identified key molecular players in the bead-enhanced Ca^{2+} response: increased integrin ligation by substrate ECM triggered ATP release and activation of P2X—but not Piezo1—ion channels. The resultant Ca^{2+} influx caused dynamic changes in cell spread area.

Conclusion: This approach to safely eliciting a Ca^{2+} response with cavitation microbubbles and the uncovered mechanism by which increased integrin-ligation mediates ATP release and Ca^{2+} signaling will inform new strategies to stimulate tissues with ultrasound and shockwaves.

Key words: Intracellular calcium signaling, cavitation bioeffects, Piezo1, integrin ligation, ATP-gated P2X channel.

Introduction

Ultrasound can be focused deep in brain or other tissue to allow non-invasive imaging and therapy [1, 2]. Therapeutic applications of ultrasound include shockwave lithotripsy [3], blood-brain barrier opening [4], targeted drug and gene delivery [5, 6], tissue ablation, and induction of anti-tumor immune

responses by high-intensity focused ultrasound (HIFU) and histotripsy [7-10]. The biological effects of therapeutic ultrasound are often caused by cavitation bubbles, which induce shear and jetting flow near interfaces [11-16], leading to cell mechanotransduction and intracellular Ca^{2+} signaling. Ultrasound-

induced microbubble oscillation is attractive for its potential utility in neuromodulation and cancer immunotherapy [17, 18]. To enhance the intended therapeutic effects of ultrasound treatment, a better understanding of the underlying mechanism is needed.

Cells sense their physical environment through mechanotransduction, the process of converting mechanical forces into biochemical signals that control cell functions. Intracellular Ca^{2+} signaling plays a crucial role in mechanotransduction and regulates myriad cell processes including exocytosis, contraction, transcription, and proliferation [19, 20]. Ca^{2+} signaling is one of the earliest events in mechanotransduction under quasi-static cell loading [21-24], and has been widely studied [25-27]. However, cavitation microbubbles exert impulsive shear flow and high strain-rate loading on cells, which can elicit a Ca^{2+} response [13, 28-30]. Previous studies reported intercellular Ca^{2+} signaling in high density cell culture from femtosecond laser exposure [31, 32], or in confluent cell monolayer from single laser-induced cavitation bubble [33, 34]. There, the Ca^{2+} signaling in one cell can propagate to its neighbors via ATP release and purinergic receptors such as P2X [31]. Yet so far very few studies have investigated the mechanism of single cell intracellular Ca^{2+} signaling that results from the shear flow of cavitation bubble.

Three mechanisms are commonly observed in shear-induced mechanotransduction in single cells: 1) direct activation of mechanosensitive ion channels such as Piezo1 [35]; 2) triggered release of ATP, which activates purinoreceptors (P2X) [36]; and 3) ligation of integrins by extracellular matrix (ECM) proteins [37-40]. The first two mechanisms involve Ca^{2+} influx through ion channels; the third mechanism involves formation of focal adhesions (FAs) on the basal surface of cell and integrin-mediated signaling. Quasi-static loading of integrin-bound beads on the apical surfaces of cells can remotely alter basal focal adhesions via integrin-cytoskeleton interactions [41].

High-frequency ultrasound (30-150 MHz) has been shown to directly activate mechanosensitive ion channels without microbubbles [17, 42-44]. However, the tissue penetration depth at such high frequencies is shallow (< 5 mm), limiting *in vivo* applications. In contrast, at regular ultrasound frequencies of 1-2 MHz, microbubbles are often required to elicit a Ca^{2+} response, as shown in *C. elegans* and in human mesenchymal stem cells and HEK293T cells [17, 18, 45].

In this work we aim to elucidate the determinants of intracellular Ca^{2+} responses induced by impulsive shear flow from single cavitation

microbubbles (SCBs). We used HEK293T cells with Piezo1 genetically knocked out (P1KO) [46] or transiently transfected (P1TF). We treated the cells with integrin-binding RGD-coated microbeads together with antibodies that block integrin ligation or with a P2X purinoreceptor inhibitor to dissect which of these previously-mentioned molecular players are involved. We found that the RGD beads were required to enhance the mechanical coupling and elicit a Ca^{2+} response without membrane poration. We established that the cellular mechanical sensing induced by microbubbles is mediated by increased integrin ligation, which leads to release of extracellular ATP (eATP) and subsequent activation of P2X channels, resulting in Ca^{2+} entry and downstream dynamic cell spreading.

Materials and Methods

Cell culture, Piezo1 transfection, and cell handling

The HEK293T-P1KO cell line (human embryonic kidney cells with Piezo1 genetically knocked out) and mouse Piezo1-pIRES-EGFP in pcDNA3.1 were obtained from Jorg Grandl's lab at Duke Neurobiology and have been described previously [46-48]. P1KO cells were maintained in high-glucose DMEM with 10% heat-inactivated fetal bovine serum (FBS) and 1% penicillin/streptomycin at 37 °C and 5% CO_2 . At 48 h before SCB treatment and recording, P1KO cells were transiently transfected in a 6-well plate (the cells were seeded 8 h before transfection) in the presence of 10 μM ruthenium red and mouse Piezo1 (3 μg) using Fugene6 (Promega, Madison, WI). 20-30% of cells showed positive GFP expression indicating successful Piezo1 transfection.

Two days after transfection, cells were seeded in Au/Ti-coated dishes pre-wetted with 1 \times PBS and coated with 50 $\mu\text{g}/\text{mL}$ fibronectin to promote cell adhesion. To avoid intercellular calcium signaling, we seeded the cells with low density and only single cells were selected for SCB treatment. To assess the role of Piezo1, a mixture of P1KO and P1TF cells was seeded; these cells were distinguished by green fluorescence from GFP co-expressed with Piezo1 in P1TF cells. Cells were incubated in DMEM at 37 °C for 3 h to allow cell adhesion and spreading. The culture medium was replaced with 6 μM fura-2 AM (F1221; Thermo Fisher Scientific) in Opti-MEM (11058-021; Thermo Fisher Scientific) and incubated at 37 °C in the dark for 30 min. Several (3-5) washes with 1 \times PBS were used to remove unloaded fura-2 AM before adding media in various experiments. Propidium iodide (PI) was added at a final concentration of 100 $\mu\text{g}/\text{mL}$ to monitor cell membrane poration.

In experiments with beads, cells were incubated at 37 °C for 30 min with 6- μm carboxyl-functionalized polystyrene beads activated with water-soluble carbodiimide, precoated with BSA (2.5% in PBS) or RGD-containing peptide (Peptide-2000; 100 $\mu\text{g}/\text{mL}$ in PBS) in 1 \times PBS with Ca^{2+} (DPBS, Catalog No. 14040133, Gibco). Unattached beads were removed by washing with 1 \times PBS.

Petri dish surface coating and SCB setup

Glass-bottom petri dishes (35 mm, No. 1.5 coverslip, P35G-1.5-20-C; MatTek Corporation, Ashland, MA) were coated with a 3 nm layer of Ti and a 7nm layer of gold by electron beam evaporation to promote SCB nucleation. SCBs were produced in medium near cells by focusing a pulsed Neodymium-doped yttrium aluminum garnet (Nd:YAG) laser beam ($\lambda = 532$ nm, 5-ns pulse duration. Orion, New Wave Research) on the coated glass surface through a 20 \times objective (Fluar NA 0.75; Zeiss). We treated single cells with distance > 150 μm from each other. Only the cells facing directly to cavitation bubble and located outside of the maximum bubble rim were chosen, see Fig. 1c. As bubble induced single-cell bioeffects depend on both the maximum bubble radius R_{max} and bubble-cell distance d , we adjusted our bubble size relative to the bubble-cell distance to match $\gamma = d/R_{\text{max}}$ within desired range. The maximum bubble diameter ranges from 90 to 110 μm in this study with the laser energy around 9-11 $\mu\text{J}/\text{pulse}$. The bubble production is associated with some fiducial on the coverslip due to laser ablation of the gold coating. Therefore, we can register and trace the sheared cells with this mark on the coverslip.

Reagents and treatment for mechanistic studies of RGD bead-enhanced Ca^{2+} response

The following treatments were performed for mechanistic studies after fura-2 loading, RGD bead attachment, and washing with Ca^{2+} -free 1 \times PBS: (1) Treatment with anti-fibronectin antibodies followed protocols in the literature [40, 49]. Cells were treated with 20 $\mu\text{g}/\text{mL}$ 16G3 or 13G12 in 1 \times PBS with Ca^{2+} for 25 min at 37 °C before bubble treatment. (2) Cells were treated with Ca^{2+} -free 1 \times PBS (DPBS, Catalog No.14190144, Gibco). (3) Gd^{3+} solution (100 μM GdCl_3) in 1 \times PBS with Ca^{2+} was used. (4) For P2X channel inhibition, 30 μM iso-PPADS in 1 \times PBS with Ca^{2+} was used. (5) To deplete extracellular ATP, cells were incubated with 20 U/mL Apyrase in 1 \times PBS with Ca^{2+} for 10 min before bubble treatment in the same medium.

Determination of whether integrin ligation is upstream or downstream of eATP release

After 3 h of cell spreading on a fibronectin-coated dish, P1KO cells were incubated with 20 $\mu\text{g}/\text{mL}$ 13G12 or 16G3 in 1 \times PBS with Ca^{2+} for 25 min (37 °C). Cells were then treated with a non-hydrolyzable ATP analog, ATP- γ -S at 0 (control), 5, 10, and 40 μM for separate dishes, respectively, and Ca^{2+} response was recorded with fura-2 ratiometric imaging.

Image recording and analysis

SCB-induced intracellular Ca^{2+} transients were captured with ratiometric imaging of Fura-2 and membrane poration was monitored with the uptake of propidium iodide (PI). Glass-bottom petri dishes with fura-2-loaded cells were fixed on the translation stage of an inverted microscope (Axio Observer Z1; Zeiss). Fluorescence excitation from a 75-W xenon lamp was controlled by a monochromator (DeltaRAM X; PTI) using shutters at defined time intervals, and at excitation wavelengths of 340 and 380 nm for fura-2 imaging, 539 nm for PI imaging, and 465 nm for GFP imaging. Since PI could also be excited at 340 and 380 nm, a custom-made narrow bandwidth filter (510 ± 40 nm) was used for detection of fura-2 emission at 510 nm to avoid overlap with PI emission at 610 nm. The intracellular fura-2 and PI images were recorded by using an sCMOS camera (EDGE 5.5 CL; PCO) at a 5:1 frame ratio, with exposure times of 50 ms and 100 ms, respectively. The image recording sequence for fura-2 was similar to our previous study [30]; an interframe time (IFT) of 0.2 s for 1 min, then an IFT of 1, 2, and 5 s for 1, 1, and 2 min, respectively, for a total recording time of 300 s, during which one PI image was recorded every five frames of fura-2 images, under the control of μ Manager software (version1.4; Open Imaging).

SCB dynamics with or without bead displacement were captured by using a high-speed camera—either an Imacon 200 (DRS Hadland) or a Kirana K1 (Specialized Imaging, with SL-LU X 640 laser for illumination)—at a recording rate of 2 million frames per second with 200-ns exposure time. The triggers for laser bubble generation and high-speed image acquisition were synchronized by a delay generator (565-8c; Berkeley Nucleonics Corporation). Fluorescence excitation, filter cubes, and image recording were automatically switched between fura-2 and PI with a switching interval ~ 0.7 s by μ Manager (Figure S1). The baseline fluorescence was recorded for 10 s, followed by high-speed imaging of bubble dynamics, then a ~ 300 s sequence of fluorescence imaging of the Ca^{2+} response and PI uptake in a cell (Fig. 1F). Cell morphology was

characterized before and after bubble treatment with single-shot bright-field images. Additional details of cell preparation, bubble generation, and imaging can be found in our previous studies [30, 50].

Raw fura-2 images were corrected by background noise subtraction. The ratiometric value $F = I_{340}/I_{380}$ was calculated with MATLAB at each pixel before obtaining the averaged ratio within each cell or ROI from a manually segmented region of the cell with ImageJ. The average Ca^{2+} response was quantified as $(F-F_0)/F_0$. Time traces of $(F-F_0)/F_0$ for each cell were processed with a one-dimensional median filter in MATLAB to reduce the noise. F_0 is the fluorescence ratio calculated by averaging the data before SCB treatment. Error estimation for Ca^{2+} response amplitude $(F_p-F_0)/F_0$ is shown in *Supplementary Material*.

Cells were chosen from dishes on at least three independent days. Results were consistent across days. So data was pooled for further analysis.

Analysis of cell spread area

Cell spread area (S) was calculated from fura-2 images with MATLAB by thresholding at each combined image frame from 340 and 380 nm excitation. The emissions from these two wavelengths have opposite trends of fluorescence change; therefore, adding them for thresholding can reduce artifacts from fluorescence intensity change. The spread areas from the image frames before bubble treatment were averaged (S_0) for normalization: $S_n = S/S_0$. Time traces of normalized cell spread area S_n were processed with the one-dimensional median filter to reduce noise. The error analysis for cell spread area reduction is shown in *Supplementary Material*.

PIV experiments and analysis

Polystyrene beads (2 μm) in $1\times$ PBS were used as tracers to map the flow field produced by SCBs. SCB dynamics and tracer bead movements were recorded by a Kirana camera with SL-LUX640 laser for illumination at 2 million frames per second and 100-ns exposure time. High-speed image sequences were analyzed offline using a commercial PIV software (DaVis 7.2; LaVision), then post-processed with MATLAB to obtain the time evolution of the flow velocity at different γ . For PIV software processing, the image field (370 \times 370 μm) was divided into multiple interrogation windows of 20 \times 20 μm each with 50% overlap, and multipass iterations and regional filters were applied to reduce the error in velocity field measurement [29].

Immunostaining of focal adhesions

Cells were fixed with 4% formaldehyde for 10 min, permeabilized with 0.1% Triton X100 for 5

min, and blocked with 2% BSA for 1 h. Cells were then incubated with primary antibodies to vinculin (Sigma V9131) or paxillin (Abcam 32084) for 2 h, labeled with secondary antibodies (30 min), and imaged via fluorescence microscopy (Olympus IX83, UPlanSApo 60 \times /NA1.35 objective).

Results

Impulsive shear flow induced by single cavitation bubbles

SCBs stimulated a mixture of isolated P1KO and P1TF cells simultaneously, increasing the throughput of the experiment. This experimental setup allowed us to assess the response of single cells located at various distances from a single microbubble (Figure 1 A–C). As both the bubble size (e.g., maximum bubble radius R_{max}) and bubble-cell distance (d) have effects on cell membrane deformation and the resultant bioeffects [29, 51, 52], we studied the influence of both by using the normalized standoff distance $\gamma (= d/R_{\text{max}})$. For more details on the experimental setup, see Materials and Methods and *Supplementary Material*, Figure S1.

A typical SCB expands to its maximum radius in $\sim 4.5 \mu\text{s}$ then collapses, followed by a second expansion and collapse with greatly reduced strength within 20 μs (Figure 1 D and E). Particle image velocimetry (PIV) measurements revealed that the velocity of the SCB-generated impulsive radial flow decreases with increasing γ , ranging from a maximum of $\sim 6 \text{ m/s}$ at $\gamma = 1.1$ to $\sim 1.6 \text{ m/s}$ at $\gamma = 1.9$ (Figure 1E). The radial flow imposes transient shear stress on adherent cells nearby ($\gamma = 1-2$) (*Supplementary Material*, Figure S2), as shown previously [53]. Shear stress τ and its time integral decrease with increasing γ . The magnitude of shear stress integral ($\int \tau^2 dt$) is similar at the fixed γ for SCBs of different size (Figure S2). Laser-induced SCBs thus allow tuning the magnitude of shear flow applied to cells by adjusting the normalized standoff distance γ [30, 54].

Ca^{2+} influx following cell exposure to cavitation bubbles may occur either through ion channels or through poration of the plasma membrane [30]. To distinguish these pathways, we used time-elapsing fluorescence imaging to concurrently monitor SCB-induced intracellular Ca^{2+} transients and membrane poration (Figure 1F). Cell injury was assessed by PI uptake and cell morphology change.

SCB-elicited Ca^{2+} responses at various distances

As bubble may cause cell membrane poration, we first studied the bubble-cell system alone without RGD microbeads. Figure 2 presents time series images of intracellular Ca^{2+} response and PI uptake in

individual P1KO and P1TF cells exposed to SCBs at $\gamma = 1.0$ – 1.5 . Bright-field images of cell morphology before and after SCB treatment are also shown. For both P1KO and P1TF cells, distinct Ca^{2+} responses were observed depending on the cell injury. Fast Ca^{2+} responses with a short rise time and a large amplitude change were accompanied by PI uptake associated with membrane poration (Figure 2 A, C and E, red and blue traces). Slower and milder Ca^{2+} responses were accompanied by negligible PI uptake (little or no membrane poration) (Figure 2 B, D and E, orange and cyan traces). The Ca^{2+} response amplitude increased with PI uptake (Supplementary Material, Figure S3), consistent with our previous findings when using tandem bubbles to stimulate HeLa cells [30].

Since the shear flow strength decreased with γ , we examined the effect of γ on the peak Ca^{2+} response, $(F_p - F_0)/F_0$, and on PI uptake. Most cells exhibiting a

Ca^{2+} response were located within $\gamma = 1.5$ of the SCB, for both P1KO and P1TF cells (Figure 2 F and G). Ca^{2+} responses within the range of $\gamma = 1.0$ – 1.5 were further classified based as “injury response” (PI uptake), “non-injury response” (no PI uptake), and “no response”. The frequencies of these responses in P1KO and P1TF cells were similar: 53% and 41% for injury response, 5% and 6% for non-injury response, and 42% and 53% for no response for P1KO and P1TF cells, respectively (Figure 2H and Supplementary Material, Figure S3). As expected, the fraction of no-response cells increased at larger γ where shear stress was smaller (Figure 2H). Within $\gamma = 1$ – 1.5 , there were more injury than non-injury responses. Since there was no significant difference in Ca^{2+} response between Piezo1 knockout and Piezo1-expressing cells, Piezo1 does not contribute to Ca^{2+} responses elicited by SCB-induced impulsive shear flow.

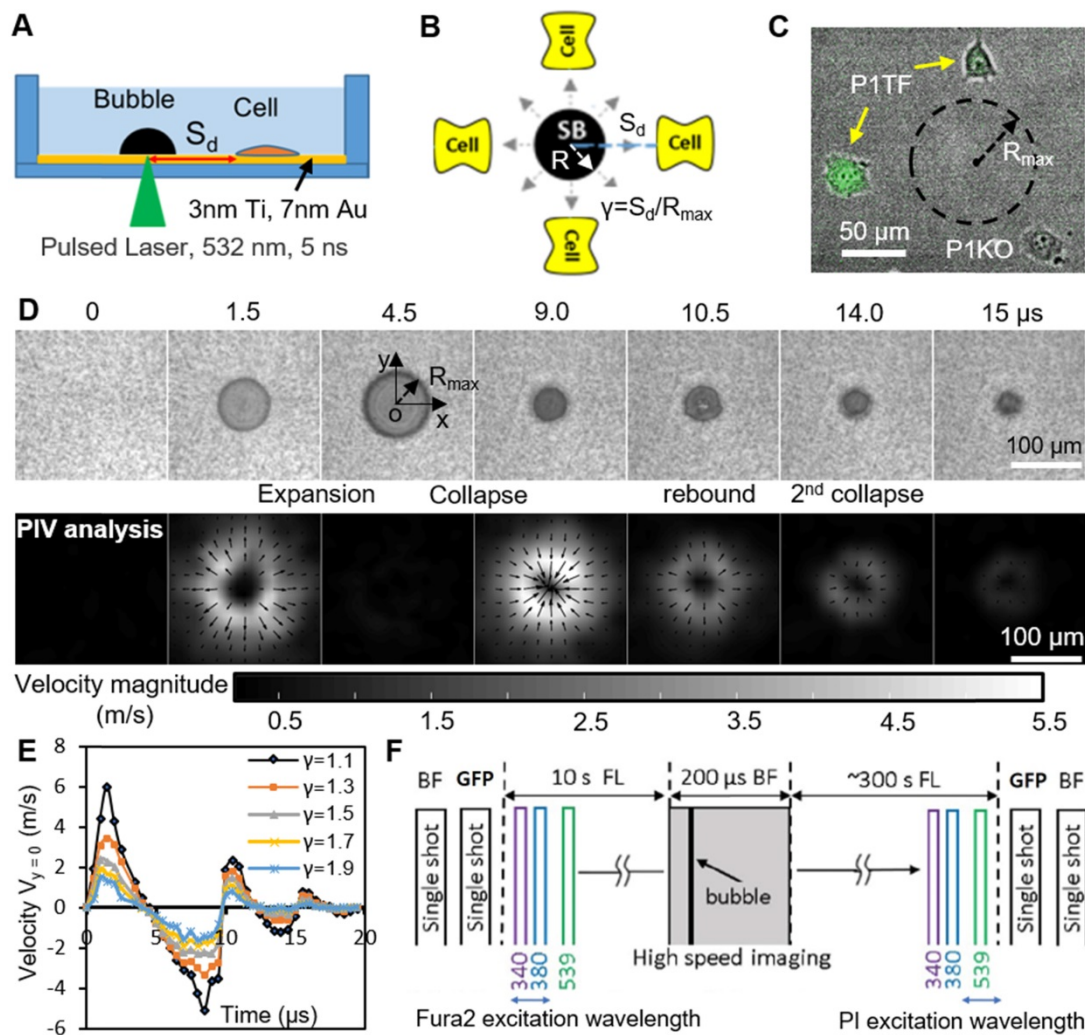


Figure 1. Experimental design. (A) A schematic of experimental setup. A laser-induced single cavitation bubble (SCB) stimulates nearby cells in a glass-bottom dish, which is coated with 3 nm Ti and 7 nm Au to enhance laser absorption while allowing optical transmission for microscopy. (B) Top view of experimental setup. S_d , standoff distance; γ , normalized standoff distance; R_{max} , maximum bubble radius. (C) Superimposed bright-field and fluorescence image of three cells with different S_d to a SCB with R_{max} indicated by black dashed line. A mixture of stable Piezo1-knockout cells (P1KO) and cells transiently transfected with GFP-Piezo1 (P1TF) was used. (D) High-speed images of bubble dynamics (upper panel) and velocity field from particle image velocimetry (PIV) (lower panel). (E) Time evolution of the SCB-generated impulsive radial flow velocity along a horizontal axis ($y = 0$) through the bubble center. Outward velocity is positive, inward velocity is negative. The velocity amplitude decreases with γ . (F) Recording sequence: bright-field imaging of cell morphology, GFP imaging of Piezo1 expression, fluorescence imaging to simultaneously monitor intracellular Ca^{2+} transients (340- and 380-nm excitation) and membrane poration (539-nm excitation), and high-speed imaging of SCB dynamics.

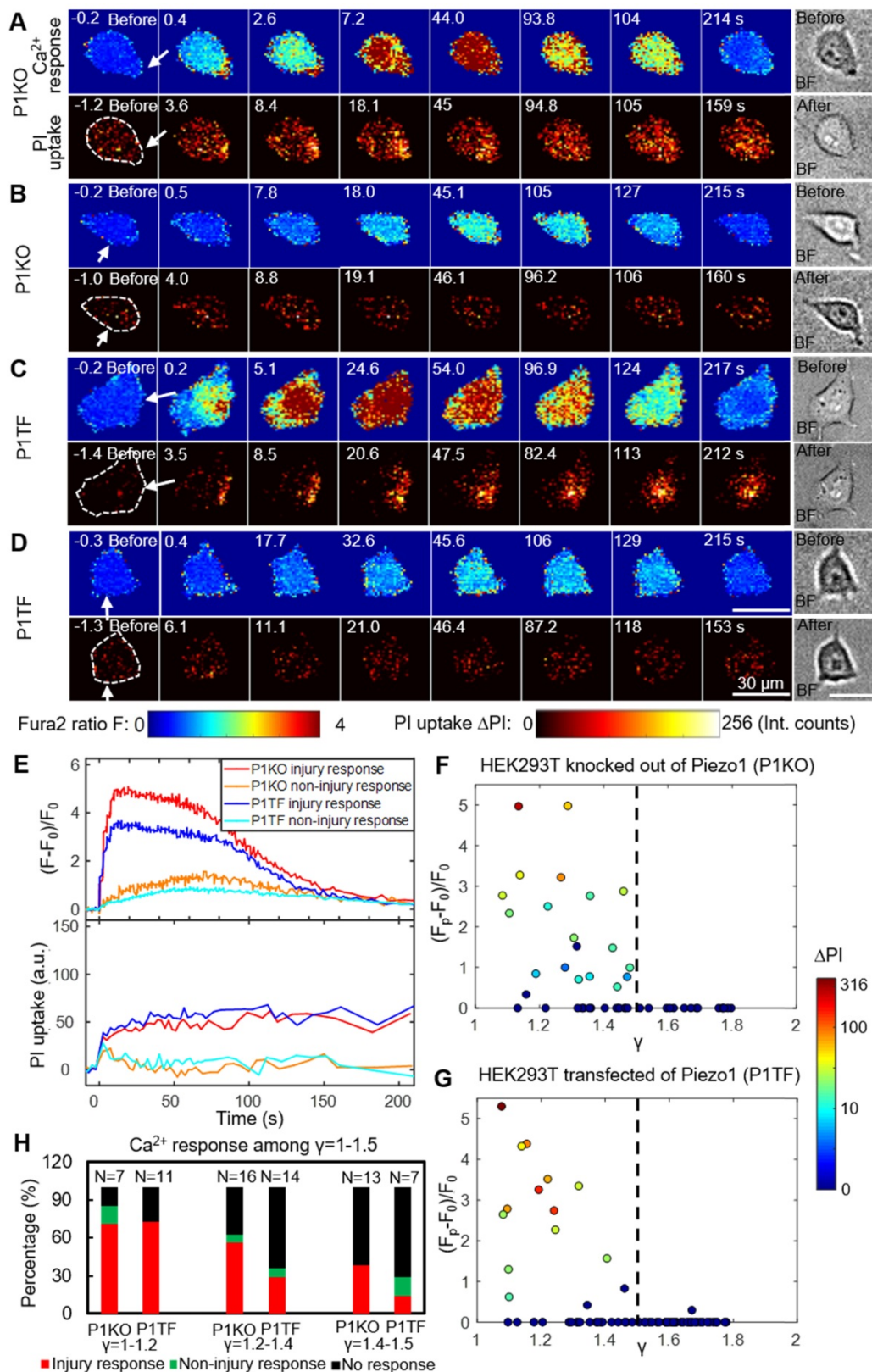


Figure 2. Intracellular Ca^{2+} response and PI uptake in SCB-stimulated cells. (A–D) Time series showing intracellular Ca^{2+} response (top rows) and PI uptake (bottom rows) in representative individual cells with membrane poration (A, C) or without membrane poration (B, D), for Piezo1 knockout cells (P1KO) (A–B) and cells transiently expressing Piezo1 (P1TF) (C–D). Right: Single-shot bright-field images of cells before and after SCB treatment. The white arrow indicates the direction of radial expansion of the SCB at the location closest to the cell. Left: The cell contour before treatment is outlined with white dashed lines in the first PI image. Cells were exposed to SCB at $t = 0$. Scale bars, 30 μ m. (E) Temporal profiles of averaged intracellular Ca^{2+} response and PI uptake inside each cell shown in A–D. (F) and (G) Peak intracellular Ca^{2+} response (circles) versus the normalized standoff distance for P1KO and P1TF cells. PI uptake values are color-coded. Almost all elicited Ca^{2+} responses occurred at $\gamma = 1-1.5$. (H) Overall Ca^{2+} response probability at $\gamma = 1-1.5$, including cells with an injury response (red), non-injury response (green), and no response/no injury (black) at different ranges of γ (1–1.2, 1.2–1.4, and 1.4–1.5). N indicates the number of cells in each group.

Enhancing Ca²⁺ responses without cell membrane poration by using RGD beads

An alternative approach to elicit a Ca²⁺ response is to enhance the mechanical load applied to cells at normalized standoff distances at which no membrane poration occurs ($\gamma = 1.5\text{--}1.8$). Informed by our previous study, we explored the effects of treating the cells with 6- μm diameter RGD-coated polystyrene microbeads [30]. RGD is widely used to bind integrins. In this way, the local drag enhanced by the microbeads on the cell apical surface can be transmitted into cells through the RGD-integrin link.

Figure 3A depicts a high-speed imaging sequence of SCB-cell interaction and the resultant displacement of RGD microbeads attached to the cell. Enlarged images (Figure 3B) show that the bead closest to the bubble was displaced significantly from its original position. The bead moved away from its

original position during bubble expansion, and back to its original position following bubble collapse, over a period of $\sim 22 \mu\text{s}$. The corresponding time-elapse images of Ca²⁺ response and PI uptake (Figure 3C) indicate a non-injury Ca²⁺ response.

Attachment of RGD beads enhanced the probability of eliciting a Ca²⁺ response at $\gamma = 1.5\text{--}1.8$ (Figure 3E). Without RGD beads, none of the 16 P1KO cells and only 1 out of 38 P1TF cells showed a Ca²⁺ response at this distance (Figure 3D). Notably, no PI uptake was observed in the RGD bead-treated cells—all Ca²⁺ responses were non-injury, for both P1KO and P1TF cells. The fraction of cells showing a Ca²⁺ response increased significantly, from 0% without beads to 42% with beads ($p < 0.01$) for P1KO, and from 2.6% to 19% ($p < 0.05$) for P1TF (Figure 3F). No statistically significant difference was found between P1KO and P1TF cells ($p > 0.05$).

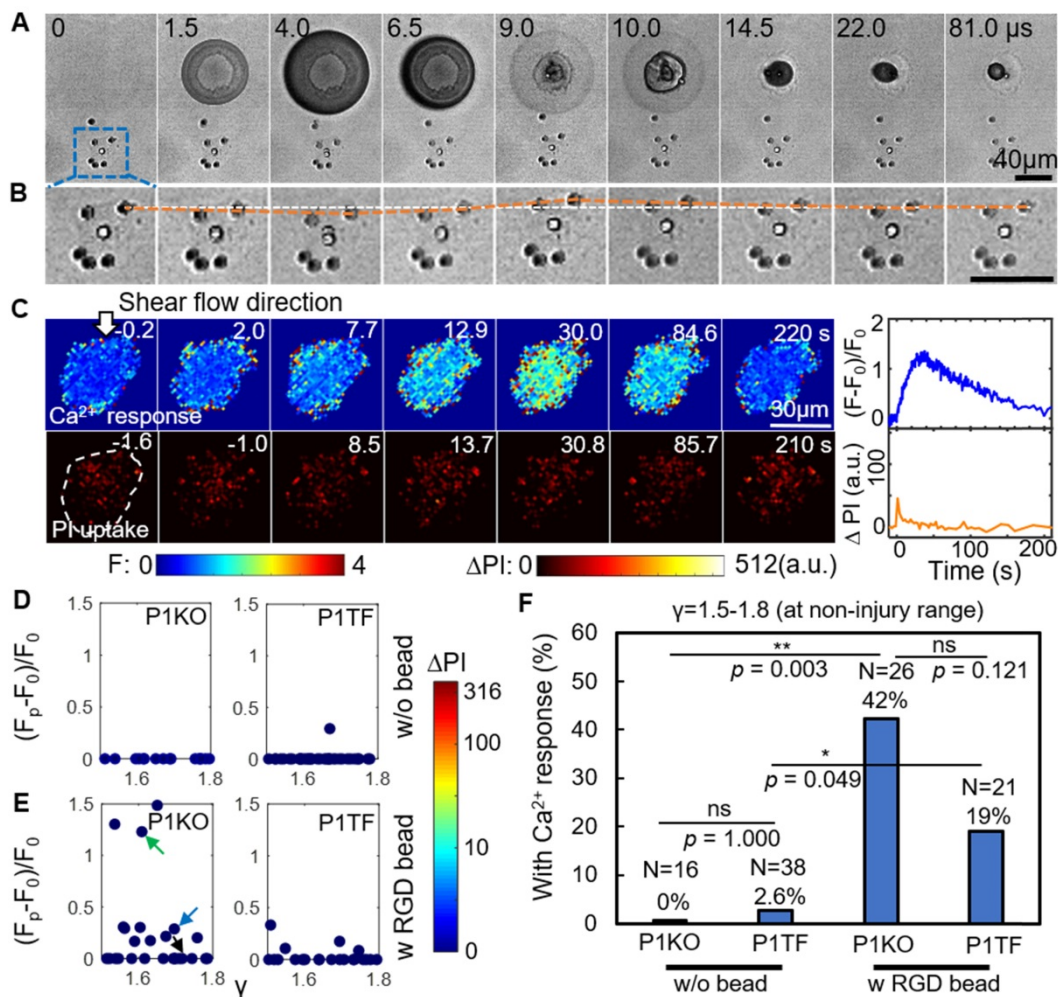


Figure 3. RGD beads enhance the Ca²⁺ response in the non-injury range of SCB treatment ($\gamma = 1.5\text{--}1.8$). (A) Image sequences from high-speed imaging showing an SCB-cell interaction with RGD beads attached to integrins on the cell apical surface. (B) Enlarged image sequence corresponding to the dashed box in A, showing displacement of the bead closest to the center of the SCB (upper right of the cell). The white line indicates the bead's original position; the orange line indicates its position at subsequent time points. (C) Left: Time-elapse image sequences of Ca²⁺ response without PI uptake in a cell subjected to SCB treatment with RGD beads. Right: Time traces of the normalized Ca²⁺ response and PI uptake. (D) and (E) Dependency of peak Ca²⁺ response on γ with the amount of PI uptake color-coded, for P1KO and P1TF cells with and without RGD beads. $\gamma = 1.5\text{--}1.8$. No cells show PI uptake, indicating no membrane poration. (F) Percentage of P1KO and P1TF cells exhibiting a Ca²⁺ response, under SCB treatment within $\gamma = 1.5\text{--}1.8$, with or without RGD beads. * $p < 0.05$, ** $p < 0.01$, ns: not significant, Fisher's exact test. N is the number of cells in each treatment group. The p value of fisher exact probability test between the four groups is less than 0.0001.

Attaching integrin-binding microbeads is thus an efficient approach to eliciting Ca^{2+} responses without cell injury. Again, no significant difference in Ca^{2+} response between Piezo1 knockout and Piezo-expressing cells was observed, indicating Piezo1 is not involved in the Ca^{2+} response.

Increased integrin ligation to substrate ECM initiates Ca^{2+} signaling from the cell periphery

To discern the processes that initiated the Ca^{2+} response to SCB with RGD beads, we examined spatiotemporal changes in Ca^{2+} signaling within P1KO cells at normalized distances causing a non-injury response ($\gamma = 1.5\text{--}1.8$). Figure 4A shows a contour map of Ca^{2+} signaling amplitude in a representative P1KO cell. Interestingly, the Ca^{2+} signaling appeared to propagate from the cell periphery toward the center, consistent with a previous study [55]. To confirm this observation, we segmented the cell into three radial regions of interest (ROI) and measured the Ca^{2+} response, $(F-F_0)/F_0$, in each ROI versus time (Figure 4B, left). The outermost ROI reached 50% of its maximum Ca^{2+} response earlier than the center ROI (~ 7.2 s versus ~ 12.5 s), with the Ca^{2+} wave propagating from the edge to the center of the cell at ~ 2.3 $\mu\text{m}/\text{s}$ (Figure 4B, right). This speed is faster than the diffusive rate of Ca^{2+} in cell [56], indicating the Ca^{2+} wave propagated in the cytosol via a reaction–diffusion process from the endoplasmic reticulum [30].

Since cells detect extracellular mechanical stimuli through integrins and focal adhesions [40, 57], we investigated whether the Ca^{2+} response is integrin-specific. Paxillin and vinculin are adaptor proteins in focal adhesions that connect transmembrane integrins with the actin cytoskeleton [58]. Based on immunofluorescence staining before bubble treatment, both paxillin and vinculin were localized mainly at the cell periphery (Figure 4C). We examined whether integrin binding was required on the cell apical surface by comparing Ca^{2+} responses of P1KO cells exposed to beads coated with either RGD or BSA (Figure 4 D and E). BSA-coated beads non-specifically bind cell membranes but experience the same drag as RGD-coated beads. The Ca^{2+} response was significantly reduced in cells when using BSA beads, indicating that integrin-specific bead attachment was vital to the Ca^{2+} response. No Ca^{2+} response was observed when using Ca^{2+} -free medium with RGD beads (Figure 4F), indicating that the increased cytosolic Ca^{2+} was dependent upon extracellular Ca^{2+} entry.

As the dynamics of our system is not compatible with significant changes in protein expression, we focus on the interaction of integrin at cell basal surface

with the substrate ECM. Increased ligation of integrins by the substrate ECM has been associated with shear-induced mechanotransduction [37–40]. We hypothesized that increased integrin ligation may be responsible for initiating the Ca^{2+} response in our study. Therefore, we examined cell spreading as an indicator for integrin-ECM interactions following SCB treatment. We observed a transient increase in normalized cell spread area S_n immediately after SCB treatment, from 2.0 s to 2.4 s (Figure 4 A and G). A Ca^{2+} response was initiated concurrently with this increase in S_n (Figure 4 G–H). This increase in cell spread area indicates the effects are at the cell basal site, supporting our hypothesis of increased integrin ligation by substrate ECM.

SCB-induced Ca^{2+} response drives transient reduction in cell spread area

After the transient increase in cell spreading immediately following SCB treatment, the spreading area decreased and then recovered to a plateau at ~ 150 s (Figure 4G). We examined this process in detail for three P1KO cells with RGD beads at $\gamma = 1.5\text{--}1.8$ before extending the analysis. The three cells showed three different Ca^{2+} responses (Figure 5 A–C). In the two cases with non-injury responses, the minimum spreading area $(S_n)_{\min}$ was reached soon after or at nearly the same time as the Ca^{2+} peak (Figure 5 A and B). The reduction in cell spread area, $1-(S_n)_{\min}$, was greater for the cell showing the larger Ca^{2+} response ($\sim 10\%$ in Figure 5A vs. $\sim 7.5\%$ in Figure 5B), and was $< 2\%$ when there was no Ca^{2+} response (Figure 5C). To reinforce this observation, we analyzed reduction in area for additional cells under the same conditions. Figure 5D and E summarize the dependence of area reduction on Ca^{2+} response and γ , respectively. The reduction in area was $< 5\%$ for no-response cases, but got larger with increasing Ca^{2+} response, reaching a maximum of 11% (Figure 5D). No clear dependence on γ was observed for the no-response cases (Figure 5E, black). In contrast, for non-injury response cases, the reduction in area decreased with increasing γ (Figure 5E, blue). Together, the results suggest that the reduction in cell spread area is a downstream effect of the Ca^{2+} response.

We also examined whether the reduction of cell spread area occurs in other Ca^{2+} response cases. In a P1KO cell without RGD beads that exhibited an injury Ca^{2+} response, the Ca^{2+} signal rose sharply upon SCB treatment at 0 s (Figure 5F), a response that is distinct from the non-injury responses (Figure 5 A–B). However, there was little transient increase in cell spreading area. This result agreed with our previous finding [30] that extracellular Ca^{2+} influx occurred through pores in the plasma membrane in injury

response cases. Despite the different route of Ca^{2+} recovery of cell spread area following the Ca^{2+} entry, in both cases we observed a reduction and response.

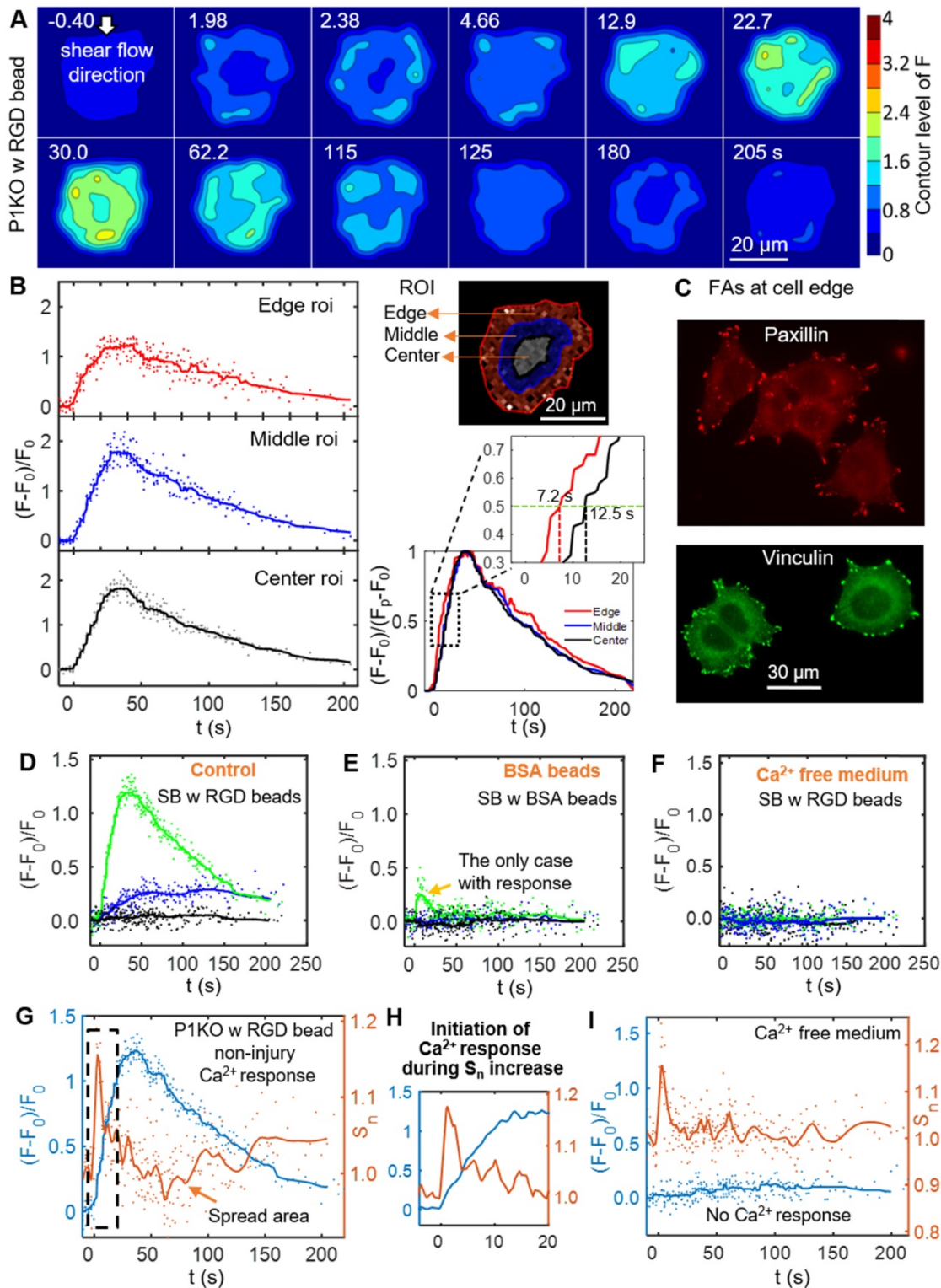


Figure 4. Initiation of the Ca^{2+} wave and localization of the focal adhesion molecules paxillin and vinculin at the cell periphery, and Ca^{2+} influx during the increase in cell spread area. (A) Surface contour of $F = I_{340}/I_{380}$ (ratiometric imaging of Ca^{2+} signaling amplitude) for a PIKO cell with RGD beads exhibiting a non-injury Ca^{2+} response (the same cell as in Figure 3C). (B) Small region analysis (edge, middle and center ROI) of the Ca^{2+} response for the cell in panel A. *Left*: Time traces of $(F-F_0)/F_0$ and median averaging. *Top right*: ROIs labels. *Bottom right*: A normalized version of the median averaging line traces is shown in the dashed box around $(F-F_0)/(F_p-F_0) = 0.5$ (horizontal dashed line). (C) Fluorescence images of focal adhesion proteins paxillin and vinculin in PIKO cells after 3 h of spreading on a gold- and FN-coated dish. (D-F) Time traces of $(F-F_0)/F_0$ for SCB-treated PIKO cells with (i) RGD beads, (ii) BSA beads, and (iii) RGD beads in Ca^{2+} -free medium. (G) Time traces of Ca^{2+} response and normalized change in cell spread area (S_n) for a SCB- and RGD-bead treated PIKO cell exhibiting a non-injury Ca^{2+} response. Solid lines indicate median averages (see Materials & Methods). (H) Enlarged image of the dashed box in panel G showing that the Ca^{2+} response is initiated during the increase in S_n . (I) Time traces of $(F-F_0)/F_0$ and S_n for a no-response case in Ca^{2+} -free medium, with a similar transient increase in S_n as seen in panel H, indicating that Ca^{2+} entry is necessary for RGD bead-enhanced response. All cases shown are cells stimulated with SCB at $\gamma = 1.5-1.8$.

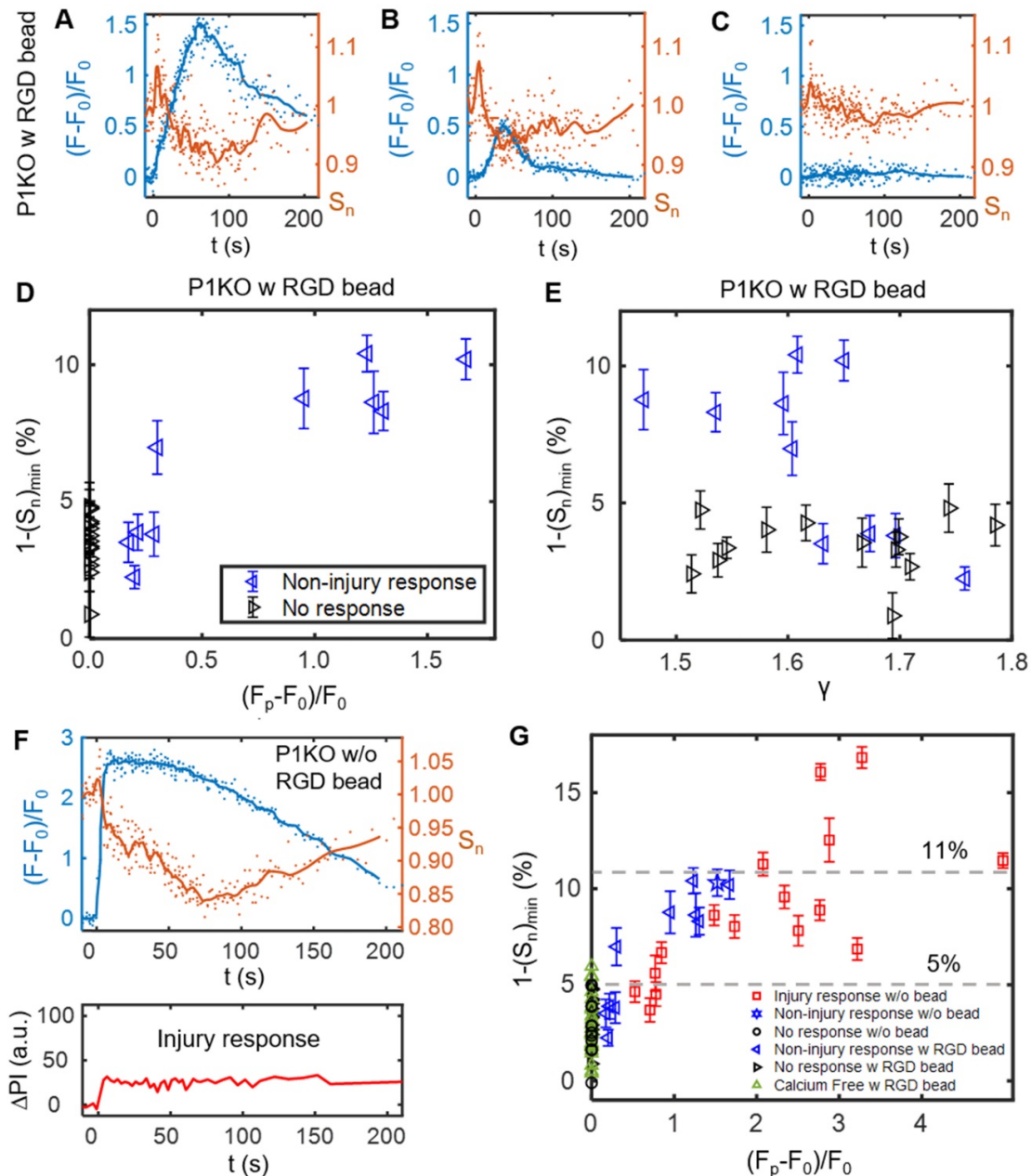


Figure 5. The SCB-induced Ca^{2+} response drives a transient reduction in cell spread area. (A-C) Change in Ca^{2+} response (blue traces) and normalized cell spread area (orange traces) versus time for three P1KO cells with RGD beads in the non-injury range ($\gamma = 1.5-1.8$). The peak Ca^{2+} response decreases from A to C. (D) Correlation of the peak Ca^{2+} response amplitude with the maximum reduction in cell spread area, $1-(S_n)_{min}$, for each P1KO cell. (E) Distribution of $1-(S_n)_{min}$ versus γ for the data shown in panel D. (F) Example of an injury Ca^{2+} response from SCB treatment of P1KO cells without RGD beads in the sub-lethal range of $\gamma = 1-1.5$, showing the change in cell spread area, Ca^{2+} response, and PI uptake over time. (G) The maximum reduction in cell spread area with Ca^{2+} response amplitude for P1KO cells with and without RGD beads. The maximum reduction in cell spread area depends on the amplitude of the Ca^{2+} response. The error bars in panel D, E and G depict the SEM.

To assess whether Ca^{2+} influx and integrin-binding RGD beads are necessary to induce the reduction in cell spreading, we extended the analysis to cases of P1KO cells with Ca^{2+} -free medium or without RGD beads (Figure 5G). There was no Ca^{2+} response in Ca^{2+} -free medium, as observed previously. In all cases with no Ca^{2+} response, the reduction in cell area was $< 6\%$ and was often comparable to the error from measurement (1.8% - 4.3% standard deviation (SD), and 0.4%-0.9% standard error of the mean (SEM)), indicated no

significant change. In contrast, for cells exhibiting a Ca^{2+} response, the reduction in cell area increased with the Ca^{2+} response amplitude and reached higher levels (up to $> 15\%$).

This analysis suggested that the transient decrease in cell spread area is a downstream effect of the Ca^{2+} response; i.e. cell spreading is a result of ‘inside-out’ signaling from regulation of cell adhesion by increased intracellular Ca^{2+} . Additional analysis of our previous data also showed transient reduction in cell spread area for tandem bubble-treated HeLa cells

with or without RGD beads, which had a Ca^{2+} response [30] (*Supplementary Material*, Figure S4). This reduction in area may be caused by myosin-II-dependent cell contraction [49] and/or intracellular Ca^{2+} -dependent calpain activation that leads to focal adhesion disassembly [59].

RGD bead-enhanced Ca^{2+} response requires new integrin ligation and subsequent extracellular ATP release

We investigated whether new ligation of integrins at the cell-ECM substrate interface is necessary to initiate the Ca^{2+} response. After P1KO cells had spread on fibronectin-coated dishes, the fibronectin-specific antibody 16G3 was added to block any new integrin $\alpha_v\beta_3$ and $\alpha_5\beta_1$ binding sites. In this way, the cells could only maintain previously established integrin-ECM connections during SCB treatment. A non-blocking fibronectin-specific antibody, 13G12, was used as a control. These antibodies are well-validated and can be taken as direct evidence for the role of integrin ligation [40, 49]. Treatment with 16G3 completely suppressed the RGD bead-enhanced Ca^{2+} response, while 13G12 had no significant effect ($p > 0.05$) on the Ca^{2+} response (Figure 6A and *Supplementary Material*, Figure S5A&B). 42% of P1KO cells showed a non-injury Ca^{2+} response with RGD beads (Figure 6B). Extracellular Ca^{2+} influx is essential in these responses, as shown by using Ca^{2+} -free medium (Figure 5G and Figure 6B). Moreover, a similar increase in S_n occurred but was not associated with a cytosolic increase in Ca^{2+} (Figure 4I), suggesting that not only integrin ligation but also extracellular Ca^{2+} entry is required to get Ca^{2+} response.

Gd^{3+} was shown previously to block both mechanosensitive ion channels and the ligand-gated P2X channel [60]; in our study, addition of 100 μM Gd^{3+} also significantly suppressed the Ca^{2+} response (Figure 6B and *Supplementary Material*, Figure S5C). Since Piezo1 was not critically involved under the impulsive shear flow (Figure 3F and Table S1), we hypothesized that the P2X channel was vital for the extracellular Ca^{2+} influx. P2X channels were responsible for shear stress-generated Ca^{2+} waves that propagated from the edge to the center of rat atrial myocytes [55]. Our hypothesis was supported by adding the P2X channel-specific blocker pyridoxal phosphate-6-azophenyl-2',5'-disulfonic acid (iso-PPADS, 30 μM), which eliminated the Ca^{2+} response (Figure 6B and *Supplementary Material*, Figure S5D).

P2X is an ATP-gated channel. We depleted eATP with 20 U/mL apyrase (an ATP-diphosphatase) and found that the Ca^{2+} response was completely

suppressed (Figure 6B and *Supplementary Material*, Figure S5E), reinforcing the hypothesis that P2X activation mediates Ca^{2+} influx following SCB treatment. We next established the causality between integrin ligation and eATP release, as both are required for the non-injury Ca^{2+} response. If integrin ligation is downstream of eATP release, the Ca^{2+} response following eATP stimulation should be affected by blocking integrin-ECM binding sites with 16G3 antibody. We observed a dose-dependent increase in the Ca^{2+} response with ATP- γ -S treatment (Figure 6 C and D). However, there was no significant difference in the Ca^{2+} response between 16G3- and 13G12-treated cells stimulated with ATP- γ -S, suggesting that integrin ligation is upstream of eATP release, consistent with previous studies [61-63].

Altogether, our results suggest the following model for the SCB-elicited Ca^{2+} response (Figure 6E): SCB-induced shear force is exerted on integrins on the cell apical surface by pulling on RGD-coated beads, causing new ligation of integrins by ECM proteins at the cell basal surface, which in turn triggers cellular release of eATP, which opens P2X ion channels, allowing Ca^{2+} influx that regulates a dynamic change in cell spreading.

Discussion

In therapeutic ultrasound and shockwave applications, the shear force experienced by cells likely involves a high strain rate [13, 64]. The effects of this impulsive shear force on single cell mechanotransduction and Ca^{2+} signaling have not been previously examined. In this study we developed a system in which laser-generated SCBs produce impulsive shear flow on multiple isolated cells nearby, allowing control of the normalized standoff distance between SCB and the cells, and used this system to dissect the key mechanisms underlying the elicited Ca^{2+} response.

In general, shear-induced mechanotransduction can be mediated by several different intracellular or extracellular structures, including mechanosensitive ion channels, purinergic receptors, and integrins, ECM [48, 65, 66]. By attaching integrin-binding RGD microbeads to the cell apical surface, we reliably elicited Ca^{2+} signaling at normalized SCB-cell distances that did not cause membrane poration. Compared to the more gently varying shear stress induced by the flow alone, the displacement of the microbeads provides a localized source of mechanical stretch on the cell membrane. This enhanced mechanical loading led to increased integrin ligation to the substrate ECM, triggering eATP release that activated ATP-gated P2X channels, and resulting in Ca^{2+} influx and downstream signaling. This approach

is also effective under impulsive jetting flow from tandem bubbles [30]. There, a similar integrin ligation mechanism is suggested for non-injury response as the Ca^{2+} signaling initiated during the transient increase of the spread area. The involvement of integrin ligation by ECM and eATP release due to high strain rate loading has not been reported before. Moreover, under the same experimental conditions, BSA-coated beads did not induce Ca^{2+} signaling, suggesting that the signaling is not due to shear force transferred to the cell membrane or cell as a whole. Instead, mechanical transmission via integrins, likely

linked to the cell basal surface via the cytoskeleton [41], appears to be necessary to transfer the stimulus to cell basal sites for activation of integrin-ligation and Ca^{2+} signaling. It is worth noting that new integrin ligation could happen at the RGD microbead surface or at the fibronectin-coated glass surface. We have focused on the glass surface as it is a larger surface area. Moreover, we have found that Ca^{2+} response was initiated during transient increase in cell spread area, indicating new ligation of integrin to substrate ECM leads to Ca^{2+} signaling.

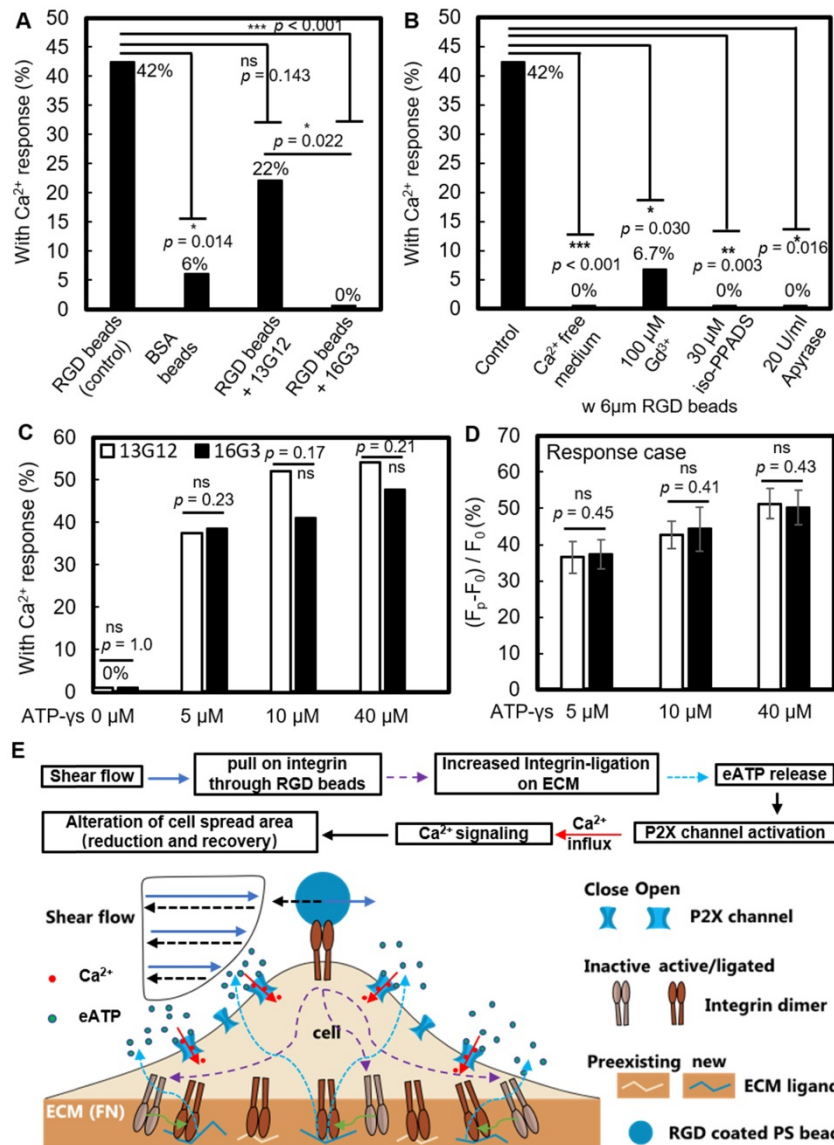


Figure 6. RGD bead enhancement of the non-injury Ca^{2+} response requires new integrin ligation and subsequent eATP release. (A) Percentage of non-injury Ca^{2+} response for SCB-treated PIKO cells at $\gamma = 1.5$ -1.8 with (i) RGD beads, N = 26; (ii) BSA beads, N = 17; (iii) RGD beads plus non-integrin-blocking anti-fibronectin antibody 13G12 (20 $\mu g/mL$), N = 23; and (iv) RGD beads plus integrin-blocking antibody 16G3 (20 $\mu g/mL$), N = 24. (B) Percentage of non-injury Ca^{2+} response in PIKO cells with RGD beads with: (i) no additional treatment (control), N = 26; (ii) Ca^{2+} -free medium, N = 26; (iii) 100 μM Gd^{3+} ($GdCl_3$), N = 15; (iv) 30 μM iso-PPADS (P2X channel inhibitor), N = 16; and (v) apyrase (20 U/ml) (depleting eATP), N = 10. (C-D) PIKO cells were treated with antibody 13G12 (white bars) or 16G3 (black bars) (20 $\mu g/mL$) after spreading on fibronectin-coated glass, then treated with different concentrations of ATP- γ -S in 1x PBS with Ca^{2+} . The resulting percentage of Ca^{2+} response is shown in panel C); the average normalized Ca^{2+} response is shown in panel D (error bar indicates SEM). The total number of cells tested in panel C was N = 24, 24, 25, and 24 for 13G12 at 0, 5, 10, and 40 μM ATP- γ -S, respectively; N = 26, 26, 22, and 21 for 16G3 at 0, 5, 10, and 40 μM ATP- γ -S, respectively. The number of cells tested in panel D was N = 9, 13, and 13 for 13G12; N = 10, 9, and 10 for 16G3 at 5, 10, and 40 μM ATP- γ -S. * $p < 0.05$, *** $p < 0.001$. P-values were calculated with two-tailed Fisher's exact test in A-C, and one-tailed student's t test in D. The p value of fisher exact probability test is less than 0.001 between the four groups in (A) and less than 0.0001 between the five groups in (B). (E) Schematic showing overall mechanotransduction process and key molecular players.

The mechanosensitive ion channel Piezo1 has been previously implicated in Ca^{2+} responses in cells stimulated by quasi-static shear flow [35, 67]. However, we observed no significant difference in Ca^{2+} response between Piezo1 knockout and Piezo1-expressing HEK293T cells, either with or without RGD beads under impulsive shear flow, indicating that Piezo1 is not involved under this shear loading regime. In general, Piezo1 enhances mechanotransduction at low strain rates and longer duration stimulations [17, 43, 44, 67, 68], but not at high strain rates due to impulsive shear flow from cavitation microbubbles, as shown here. The involvement of Piezo1 appears to be a key factor distinguishing cell mechanotransduction at different loading regimes.

Some elements of the mechanism identified in our study have been reported previously for ultrasound-induced mechanotransduction. For example, 2 MHz ultrasound alone did not evoke a Ca^{2+} response in HEK293T cells transfected with Piezo1, but did evoke a response when integrin-binding microbubbles were attached to the cell membrane [17]. The importance of integrins in transducing mechanical forces produced by ultrasound has also been suggested by the effect of therapeutic low-intensity pulsed ultrasound (LIPUS) on cell motility via integrin-ECM adhesions [66]. In our study, eATP release and purinergic signaling was important in Ca^{2+} response, and were also shown to be important in Ca^{2+} signaling in human mesenchymal stem cells stimulated using low-intensity ultrasound [69]. Despite this scattered evidence, the molecular cascade identified in our study has not been reported in the context of ultrasound or cavitation microbubble induced mechanotransduction.

It is worth mentioning that Ca^{2+} response also can be evoked by ultrasound excitation of functionalized microbubbles, which were attached to cell membrane via RGD-integrin binding (e.g., the so called ultrasound/acoustic tweezers with stable cavitation) [70]. Therefore, both stable, as used in other studies, and inertial cavitation, as used in our study, could stimulate cellular Ca^{2+} response. Future studies are warranted to determine which method is better for each specific application.

Compared to the current ultrasound/acoustic tweezers, the main difference is the robustness of our microbeads approach, where the beads can be stimulated multiple times without losing its mechanical integrity. In contrast, coated microbubbles used in acoustic tweezers may rupture or gradually leak out its gas content during/after insonification that lasts longer. Besides, the microstreaming

produced by coated microbubble oscillation will be much weaker than that produced by inertial cavitation bubble, leading to a significantly diminished effective range of the approach. On the other hands, optical tweezers have also been used to elicit intracellular Ca^{2+} responses [23]. However, it usually moves the microbeads on cell membrane in a quasi-static manner (millisecond to second range) while our approach impulsively displaces the beads within much shorter duration (tens of microseconds).

Conclusions

Our results establish that applying forces to integrins and activating ATP-gated P2X ion channels is an efficient approach to elicit non-injury Ca^{2+} response in cavitation bubble-generated impulsive shear flow. We anticipate that the insights from this study will enable development of new strategies for better use of therapeutic ultrasound. First, this strategy does not require expression of exogenous mechanosensitive ion channels such as Piezo1 or MscL I92L [42], which were activated primarily by high-frequency ultrasound (tens of MHz), which has a limited penetration depth *in vivo*. Second, since expression of integrins and P2X is widespread in mammalian brain, muscle, and other tissues [65], ultrasound alone or mediated by cavitation could stimulate these tissues through a similar mechanism. In addition to neurotransmission and neuromodulation, P2X purinergic signaling is involved in cell proliferation, differentiation, motility, and apoptosis and in tissue regeneration and wound healing in muscle and other tissues [71, 72]. By applying impulsive shear force with ultrasonic cavitation bubbles that deforms the native ECM (thus pulling on integrins), we may be able to trigger the P2X purinergic signaling pathway and modulate cell functions in the brain and other tissues. Overall, these results provide insight into both the mechanism of cavitation bubble-mediated cell stimulation and strategies for improving therapeutic ultrasound applications in tissue stimulation.

Abbreviations

SCBs: single cavitation microbubbles; HEK293T: human embryonic kidney 293T cells; P1KO: piezo1 knock out; P1TF: Piezo1 transfected; GFP: green fluorescence protein; PI: propidium iodide; RGD: Arginylglycylaspartic acid; ECM: extracellular matrix; FAs: focal adhesions; eATP: extracellular Adenosine triphosphate; LIPUS: low-intensity pulsed ultrasound; HIFU: high-intensity focused ultrasound; PBS: phosphate-buffered saline; FBS: fetal bovine serum; BSA: bovine serum albumin; DMEM: Dulbecco's Modified Eagle's Medium; iso-PPADS:

pyridoxalphosphate-6-azophenyl-2',5'-disulfonic acid.

Supplementary Material

Supplementary figures and tables.

<http://www.thno.org/v11p6090s1.pdf>

Acknowledgments

The authors thank Prof. Jorg Grandl from Duke Neurobiology for providing the P1KO cell line and Piezo1 plasmid, and Dr. Kenneth Yamada from National Institutes of Health for the 16G3 and 13G12 antibodies. The authors thank Ashley Henderson for technical support, and Amanda Lewis for guidance in P1KO cell culture and Piezo1 plasmid transfection and helpful discussions. This work was supported by the National Institutes of Health Grant 5R37-DK052985-23.

Competing Interests

The authors have declared that no competing interest exists.

References

- Miller DL, Smith NB, Bailey MR, Czarnota GJ, Hynynen K, Makin IR, et al. Overview of therapeutic ultrasound applications and safety considerations. *J Ultrasound Med.* 2012; 31: 623-34.
- Gebauer D, Mayr E, Orthner E, Ryaby JP. Low-intensity pulsed ultrasound: effects on nonunions. *Ultrasound Med Biol.* 2005; 31: 1391-402.
- Zhong P. Shock wave lithotripsy. In: Delale CF, editor. *Bubble dynamics and shock waves*: Springer Berlin Heidelberg. 2013; p:291-338.
- Hynynen K, McDannold N, Sheikov NA, Jolesz FA, Vykhodtseva N. Local and reversible blood-brain barrier disruption by noninvasive focused ultrasound at frequencies suitable for trans-skull sonications. *Neuroimage.* 2005; 24: 12-20.
- Fan Z, Liu H, Mayer M, Deng CX. Spatiotemporally controlled single cell sonoporation. *Proc Natl Acad Sci U S A.* 2012; 109: 16486-91.
- Frenkel V. Ultrasound mediated delivery of drugs and genes to solid tumors. *Adv Drug Deliv Rev.* 2008; 60: 1193-208.
- Hu Z, Yang XY, Liu Y, Sankin GN, Pua EC, Morse MA, et al. Investigation of HIFU-induced anti-tumor immunity in a murine tumor model. *J Transl Med.* 2007; 5: 34.
- Kennedy JE. High-intensity focused ultrasound in the treatment of solid tumours. *Nat Rev Cancer.* 2005; 5: 321-7.
- Wu F, Wang ZB, Lu P, Xu ZL, Chen WZ, Zhu H, et al. Activated anti-tumor immunity in cancer patients after high intensity focused ultrasound ablation. *Ultrasound Med Biol.* 2004; 30: 1217-22.
- Roberts WW, Hall TL, Ives K, Wolf JS, Fowlkes JB, Cain CA. Pulsed cavitation ultrasound: A noninvasive technology for controlled tissue ablation (histotripsy) in the rabbit kidney. *J Urol.* 2006; 175: 734-8.
- Mohammadzadeh M, Li FF, Ohl CD. Shearing flow from transient bubble oscillations in narrow gaps. *Phys Rev Fluids.* 2017; 2: 014301.
- Lokhandwalla M, Sturtevant B. Mechanical haemolysis in shock wave lithotripsy (SWL): I. Analysis of cell deformation due to SWL flow-fields. *Phys Med Biol.* 2001; 46: 413-37.
- Li FF, Chan CU, Ohl CD. Yield strength of human erythrocyte membranes to impulsive stretching. *Biophys J.* 2013; 105: 872-9.
- Wu JR. Shear stress in cells generated by ultrasound. *Prog Biophys Mol Bio.* 2007; 93: 363-73.
- VanBavel E. Effects of shear stress on endothelial cells: Possible relevance for ultrasound applications. *Prog Biophys Mol Bio.* 2007; 93: 374-83.
- Ohl SW, Klaseboer E, Khoo BC. Bubbles with shock waves and ultrasound: a review. *Interface Focus.* 2015; 5: 20150019.
- Pan Y, Yoon S, Sun J, Huang Z, Lee C, Allen M, et al. Mechanogenetics for the remote and noninvasive control of cancer immunotherapy. *Proc Natl Acad Sci U S A.* 2018; 115 (5): 992-997.
- Ibsen S, Tong A, Schutt C, Esener S, Chalasani SH. Sonogenetics is a non-invasive approach to activating neurons in *Caenorhabditis elegans*. *Nat Commun.* 2015; 6: 8264.
- Berridge MJ, Lipp P, Bootman MD. The versatility and universality of calcium signalling. *Nat Rev Mol Cell Biol.* 2000; 1: 11-21.
- Clapham DE. Calcium signaling. *Cell.* 2007; 131: 1047-58.
- Rand RP. Mechanical properties of the red cell membrane. II. viscoelastic breakdown of the membrane. *Biophys J.* 1964; 4: 303-16.
- Rand RP, Burton AC. Mechanical properties of the red cell membrane. I. membrane stiffness and intracellular pressure. *Biophys J.* 1964; 4: 115-35.
- Zhang H, Liu KK. Optical tweezers for single cells. *J R Soc Interface.* 2008; 5: 671-90.
- Puig-de-Morales-Marinkovic M, Turner KT, Butler JP, Fredberg JJ, Suresh S. Viscoelasticity of the human red blood cell. *Am J Physiol Cell Physiol.* 2007; 293: C597-605.
- Benavides Damm T, Egli M. Calcium's role in mechanotransduction during muscle development. *Cell Physiol Biochem.* 2014; 33: 249-72.
- el Haj AJ, Walker LM, Preston MR, Publicover SJ. Mechanotransduction pathways in bone: calcium fluxes and the role of voltage-operated calcium channels. *Med Biol Eng Comput.* 1999; 37: 403-9.
- Orr AW, Helmke BP, Blackman BR, Schwartz MA. Mechanisms of mechanotransduction. *Dev Cell.* 2006; 10: 11-20.
- Li F, Chan CU, Ohl CD. Rebuttal to a comment by Richard E. Waugh on our article "Yield strength of human erythrocyte membranes to impulsive stretching". *Biophys J.* 2014; 106: 1832-3.
- Yuan F, Yang C, Zhong P. Cell membrane deformation and bioeffects produced by tandem bubble-induced jetting flow. *Proc Natl Acad Sci U S A.* 2015; 112: E7039-47.
- Li F, Yang C, Yuan F, Liao D, Li T, Guilak F, et al. Dynamics and mechanisms of intracellular calcium waves elicited by tandem bubble-induced jetting flow. *Proc Natl Acad Sci U S A.* 2018; 115: E353-E62.
- Zhao Y, Zhang Y, Zhou W, Liu X, Zeng S, Luo Q. Characteristics of calcium signaling in astrocytes induced by photostimulation with femtosecond laser. *J Biomed Opt.* 2010; 15: 035001.
- He H, Wang S, Li X, Li S, Hu M, Cao Y, et al. Ca²⁺ waves across gaps in non-excitable cells induced by femtosecond laser exposure. *Appl Phys Lett.* 2012; 100: 173704.
- Compton JL, Luo JC, Ma H, Botvinick E, Venugopalan V. High-throughput optical screening of cellular mechanotransduction. *Nat Photonics.* 2014; 8: 710-5.
- Luo JC, Botvinick EL, Venugopalan V. Reply to 'Mechanism for microtunami-induced intercellular mechanosignalling'. *Nat Photonics.* 2015; 9: 624-5.
- Cinar E, Zhou S, DeCoursey J, Wang Y, Waugh RE, Wan J. Piezo1 regulates mechanotransductive release of ATP from human RBCs. *Proc Natl Acad Sci U S A.* 2015; 112: 11783-8.
- Yamamoto K, Korenaga R, Kamiya A, Ando J. Fluid shear stress activates Ca²⁺ influx into human endothelial cells via P2X4 purinoceptors. *Circ Res.* 2000; 87: 385-91.
- Schwartz MA, Schaller MD, Ginsberg MH. Integrins: emerging paradigms of signal transduction. *Annu Rev Cell Dev Biol.* 1995; 11: 549-99.
- Hoffman BD, Grashoff C, Schwartz MA. Dynamic molecular processes mediate cellular mechanotransduction. *Nature.* 2011; 475: 316-23.
- Katsumi A, Naoe T, Matsushita T, Kaibuchi K, Schwartz MA. Integrin activation and matrix binding mediate cellular responses to mechanical stretch. *J Biol Chem.* 2005; 280: 16546-9.
- Jalali S, del Pozo MA, Chen KD, Miao H, Li YS, Schwartz MA, et al. Integrin-mediated mechanotransduction requires its dynamic interaction with specific extracellular matrix (ECM) ligands. *Proc Natl Acad Sci U S A.* 2001; 98: 1042-6.
- Hu S, Chen J, Fabry B, Numaguchi Y, Gouldstone A, Ingber DE, et al. Intracellular stress tomography reveals stress focusing and structural anisotropy in cytoskeleton of living cells. *Am J Physiol Cell Physiol.* 2003; 285: C1082-90.
- Ye J, Tang SY, Meng L, Li X, Wen XX, Chen SH, et al. Ultrasonic control of neural activity through activation of the mechanosensitive channel MscL. *Nano Lett.* 2018; 18: 4148-55.
- Liao D, Li F, Lu D, Zhong P. Activation of Piezo1 mechanosensitive ion channel in HEK293T cells by 30 MHz vertically deployed surface acoustic waves. *Biochem Biophys Res Commun.* 2019; 518: 541-7.
- Prieto ML, Firouzi K, Khuri-Yakub BT, Maduke M. Activation of piezo1 but not NaV1.2 channels by ultrasound at 43 MHz. *Ultrasound Med Biol.* 2018; 44: 1217-32.
- Xue X, Hong X, Li Z, Deng CX, Fu J. Acoustic tweezing cytometry enhances osteogenesis of human mesenchymal stem cells through cytoskeletal contractility and YAP activation. *Biomaterials.* 2017; 134: 22-30.
- Lukacs V, Mathur J, Mao R, Bayrak-Toydemir P, Procter M, Cahalan SM, et al. Impaired PIEZO1 function in patients with a novel autosomal recessive congenital lymphatic dysplasia. *Nat Commun.* 2015; 6: 8329.
- Lewis AH, Grandl J. Mechanical sensitivity of Piezo1 ion channels can be tuned by cellular membrane tension. *Elife.* 2015; 4: e12088.
- Coste B, Xiao BL, Santos JS, Syeda R, Grandl J, Spencer KS, et al. Piezo proteins are pore-forming subunits of mechanically activated channels. *Nature.* 2012; 483: 176-U72.
- Muhamed I, Wu J, Sehgal P, Kong X, Tajik A, Wang N, et al. E-cadherin-mediated force transduction signals regulate global cell mechanics. *J Cell Sci.* 2016; 129: 1843-54.
- Li FF, Yuan F, Sankin G, Yang C, Zhong P. A microfluidic system with surface patterning for investigating cavitation bubble(s)-cell interaction and the resultant bioeffects at the single-cell level. *J Vis Exp.* 2017; 119: 55106.

51. Li ZG, Liu AQ, Klaseboer E, Zhang JB, Ohl CD. Single cell membrane poration by bubble-induced microjets in a microfluidic chip. *Lab Chip*. 2013; 13: 1144-50.
52. Dijkink R, Le Gac S, Nijhuis E, van den Berg A, Vermes I, Poot A, et al. Controlled cavitation-cell interaction: trans-membrane transport and viability studies. *Phys Med Biol*. 2008; 53: 375-90.
53. Rau KR, Quinto-Su PA, Hellman AN, Venugopalan V. Pulsed laser microbeam-induced cell lysis: time-resolved imaging and analysis of hydrodynamic effects. *Biophys J*. 2006; 91: 317-29.
54. Tandiono T, Klaseboer E, Ohl SW, Ow DSW, Choo ABH, Li FF, et al. Resonant stretching of cells and other elastic objects from transient cavitation. *Soft Matter*. 2013; 9: 8687-96.
55. Kim JC, Son MJ, Woo SH. Ca²⁺ signaling triggered by shear-autocrine P2X receptor pathway in rat atrial myocytes. *Cell Physiol Biochem*. 2018; 50: 2296-313.
56. Kupferman R, Mitra PP, Hohenberg PC, Wang SS. Analytical calculation of intracellular calcium wave characteristics. *Biophys J*. 1997; 72: 2430-44.
57. Sun Z, Guo SS, Fassler R. Integrin-mediated mechanotransduction. *J Cell Biol*. 2016; 215: 445-56.
58. Roca-Cusachs P, Iskratsch T, Sheetz MP. Finding the weakest link: exploring integrin-mediated mechanical molecular pathways. *J Cell Sci*. 2012; 125: 3025-38.
59. Franco SJ, Rodgers MA, Perrin BJ, Han J, Bennin DA, Critchley DR, et al. Calpain-mediated proteolysis of talin regulates adhesion dynamics. *Nat Cell Biol*. 2004; 6: 977-83.
60. Nakazawa K, Liu M, Inoue K, Ohno Y. Potent inhibition by trivalent cations of ATP-gated channels. *Eur J Pharmacol*. 1997; 325: 237-43.
61. Alvarez A, Lagos-Cabre R, Kong M, Cardenas A, Burgos-Bravo F, Schneider P, et al. Integrin-mediated transactivation of P2X7R via hemichannel-dependent ATP release stimulates astrocyte migration. *Biochim Biophys Acta*. 2016; 1863: 2175-88.
62. Leanne M, France M, Steve C, Kris C. The NLRP3 inflammasome is a pathogen sensor for invasive entamoeba histolytica via activation of $\alpha 5 \beta 1$ integrin at the macrophage-amebae intercellular junction. *PLoS Pathog*. 2015; 11: e1004887.
63. O'Brien KA, Gartner TK, Hay N, Du X. ADP-stimulated activation of Akt during integrin outside-in signaling promotes platelet spreading by inhibiting glycogen synthase kinase-3beta. *Arterioscler Thromb Vasc Biol*. 2012; 32: 2232-40.
64. Li D, Pellegrino A, Hallack A, Petrinic N, Jerusalem A, Cleveland RO. Response of single cells to shock waves and numerically optimized waveforms for cancer therapy. *Biophys J*. 2018; 114: 1433-9.
65. Seguela P, Haghighi A, Soghomonian JJ, Cooper E. A novel neuronal P2x ATP receptor ion channel with widespread distribution in the brain. *J Neurosci*. 1996; 16: 448-55.
66. Atherton P, Lausecker F, Harrison A, Ballestrem C. Low-intensity pulsed ultrasound promotes cell motility through vinculin-controlled Rac1 GTPase activity. *J Cell Sci*. 2017; 130: 2277-91.
67. Ranade SS, Qiu Z, Woo SH, Hur SS, Murthy SE, Cahalan SM, et al. Piezo1, a mechanically activated ion channel, is required for vascular development in mice. *Proc Natl Acad Sci U S A*. 2014; 111: 10347-52.
68. Qiu Z, Guo J, Kala S, Zhu J, Xian Q, Qiu W, et al. The mechanosensitive ion channel Piezo1 significantly mediates *in vitro* ultrasonic stimulation of neurons. *iScience*. 2019; 21: 448-57.
69. Yoon CW, Jung H, Goo K, Moon S, Koo KM, Lee NS, et al. Low-intensity ultrasound modulates Ca(2+) dynamics in human mesenchymal stem cells via connexin 43 hemichannel. *Ann Biomed Eng*. 2018; 46: 48-59.
70. Fan ZZ, Sun YB, Chen D, Tay D, Chen WQ, Deng CX, et al. Acoustic tweezing cytometry for live-cell subcellular modulation of intracellular cytoskeleton contractility. *Sci Rep*. 2013; 3: 2176.
71. Weihs AM, Fuchs C, Teuschl AH, Hartinger J, Slezak P, Mittermayr R, et al. Shock wave treatment enhances cell proliferation and improves wound healing by ATP release-coupled extracellular signal-regulated kinase (ERK) activation. *J Biol Chem*. 2014; 289: 27090-104.
72. Burnstock G, Verkhatsky A. Long-term (trophic) purinergic signalling: purinoceptors control cell proliferation, differentiation and death. *Cell Death Dis*. 2010; 1: e9.